JOURNAL OF AIRCRAFT
Vol. 44, No. 4, July–August 2007

Multidisciplinary Design Optimization and Data Mining for Transonic Regional-Jet Wing

Kazuhisa Chiba* and Akira Oyama†
Japan Aerospace Exploration Agency, Tokyo 182-8522, Japan
Shigeru Obayashi‡ and Kazuhiro Nakahashi§
Tohoku University, Sendai 980-8577, Japan
and
Hiroyuki Morino¶
Mitsubishi Heavy Industries, Ltd., Nagoya 455-8515, Japan

DOI: 10.2514/1.17549

A large-scale, real-world application of evolutionary multi-objective optimization is reported. The multidisciplinary design optimization among aerodynamics, structures, and aeroelasticity of the wing of a transonic regional-jet aircraft was performed using high-fidelity evaluation models. Euler and Navier–Stokes solvers were employed for aerodynamic evaluation. The commercial software NASTRAN was coupled with a computational fluid dynamics solver for the structural and aeroelastic evaluations. An adaptive range multi-objective genetic algorithm was employed as an optimizer. The objective functions were minimizations of block fuel and maximum takeoff weight in addition to drag divergence between transonic and subsonic flight conditions. As a result, nine nondominated solutions were generated and used for tradeoff analysis among three objectives. Moreover, all solutions evaluated during the evolution were analyzed using a self-organizing map as a data mining technique to extract key features of the design space. One of the key features found by data mining was the nongull wing geometry, although the present multidisciplinary design optimization results showed the inverted gull wings as nondominated solutions. When this knowledge was applied to one optimum solution, the resulting design was found to have better performance and to achieve 3.6% improvement in the block fuel compared to the original geometry designed in the conventional manner.

I. Introduction

RECENT studies on multidisciplinary design optimization (MDO) have been conducted for aircraft design [1,2]. Pure aerodynamic optimization shows wings with a low thickness-to-chord ratio and a high aspect ratio. These wings suffer undesirable aeroelastic phenomena due to their low bending and torsional stiffness. Aerostructural interactive optimization is needed to overcome these phenomena and to allow realistic aircraft design [3]. This multi-objective optimization will provide a good field for the application of evolutionary multi-objective optimization (EMO).

In Japan, a five-year research and design project has been in progress toward the development of an environmentally friendly high performance small jet aircraft under the auspices of the New Energy and Industrial Technology Development Organization (NEDO) since 2003, in which new technical features have been investigated including advanced aerodynamics, new materials, and a human centered cockpit by industry–government–university cooperation.

The objective of this study is to optimize the three-dimensional wing shape for the proposed regional-jet aircraft using evolutionary multi-objective optimization with high-fidelity simulations as collaboration between the Institute of Fluid Science (IFS), Tohoku University, and Mitsubishi Heavy Industries, Ltd. (MHI). From the optimization results, a tradeoff analysis was performed among the three objectives. Moreover, by using a data mining technique, aerostructural design knowledge for transonic regional-jet aircraft has been obtained.

In the present study, high-fidelity simulation tools, such as a Reynolds-averaged Navier–Stokes (NS) solver for aerodynamics, NASTRAN, versatile and high-fidelity commercial software, for structures and aeroelasticity were coupled together for MDO. Although the Euler/NS solver may still be too expensive for real-world design environments, it can predict complex and nonlinear flow phenomena, such as shock wave and separation, with a high degree of accuracy. Such nonlinearity will provide a severe test case for EMO. Each disciplinary objective is treated as an independent objective function on an optimizer to obtain knowledge in the design space directly. That is, this MDO is defined as a large-scale multi-objective optimization problem. Aided by the rapid progress in computer hardware, the demonstration described here will become standard design practice in the near future.

II. Multidisciplinary Design Optimization

A. Objective Functions

In this system, minimization of the block fuel at a required target range derived from aerodynamics and structures was selected as an objective function. In addition, two more objective functions were considered—minimization of the maximum takeoff weight and minimization of the difference in the drag coefficient between two Mach numbers, which are cruise Mach and target maximum operating Mach number (MMO), to prevent decrease MMO.

Presented as Paper 5080 at the AIAA 23rd Applied Aerodynamics Conference, Westin Harbour Castle, Toronto, Ontario, Canada, 6–9 June 2005; received 6 May 2005; revision received 29 August 2005; accepted for publication 8 November 2005.

*Project Researcher, Civil Transport Team, Aviation Program Group; formerly Graduate Student, Tohoku University. Member AIAA.
†Research Associate, Institute of Space and Astronautical Science; formerly Researcher, Tohoku University. Member AIAA.
‡Professor, Institute of Fluid Science. Associate Fellow AIAA.
§Professor, Department of Aeronautics and Space Engineering. Associate Fellow AIAA.
¶Research Engineer, Nagoya Aerospace Systems.

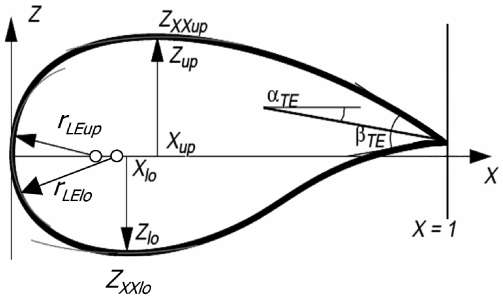

Fig. 1 Illustration of the modified PARSEC airfoil shape defined by nine design variables.

B. Geometry Definition

First, the planform was given by MHI. The front and rear spar positions were fixed in the structural shape based on the initial aerodynamic geometry. The wing structural model was substituted with shell elements.

The design variables were related to airfoil, twist, and wing dihedral. The airfoil was defined at three spanwise cross sections using the modified "PARSEC" [4] with nine design variables (x_{up}, z_{up}, $z_{xx_{\text{up}}}$, x_{lo}, z_{lo}, $z_{xx_{\text{lo}}}$, α_{TE}, β_{TE}, and $r_{\text{LE}_{\text{lo}}}/r_{\text{LE}_{\text{up}}}$) for each cross section as shown in Fig. 1. The twists were defined at six spanwise locations, and then wing dihedrals were defined at kink and tip locations. The twist center was set on the trailing edge in the present study. The entire wing shape was thus defined using 35 design variables. The detail of the design variables is summarized in Table 1. In the present study, the geometry of each individual was generated by the unstructured dynamic mesh method [5,6] using displacement from the initial geometry.

C. Constraints

The five constraints were considered in the optimizer. The first three were geometrical constraints, while the last two were constraints for flight condition as follows:

1) The distribution of the parameter Δy to describe leading-edge geometry was constrained in the spanwise direction to prevent abrupt stall characteristics. Here, Δy denotes an airfoil upper surface ordinate at 6% chord from the leading edge minus the ordinate at 0.15% chord.

2) Rear spar heights were greater than required for housing of the control surfaces.

3) The lower and upper surfaces of the spars changed monotonically in the spanwise direction.

4) The lift coefficients increased monotonically with increasing Mach number to satisfy target MLD (lift divergence Mach number).

5) The evaluated fuel for the given range was less than the wing fuel volume.

D. Optimizer

Evolutionary algorithms (EAs), particularly genetic algorithms (GAs), are based on the theory of evolution, where a biological population evolves over generations to adapt to an environment by selection, crossover, and mutation. Fitness, individuals, and genes in the evolutionary theory correspond to the objective function, design candidates, and design variables in design optimization problems, respectively.

GAs search for optima from multiple points in the design space simultaneously and stochastically. GAs can prevent the search from settling in a local optimum. Moreover, GAs do not require computing gradients of the objective function. These features lead to the following advantages of GAs coupled with computational fluid dynamics (CFD): 1) GAs have the capability of finding global optimal solutions. 2) GAs can be processed in parallel. 3) High-fidelity CFD codes can be adapted to GAs easily without any modification. 4) GAs are not sensitive to any noise that might be present in the computation.

Adaptive range multi-objective genetic algorithm (ARMOGA) [7] is an efficient multi-objective evolutionary algorithm (MOEA) designed for aerodynamic optimization and multidisciplinary design optimization problems using high-fidelity CFD solvers with large computational time. ARMOGA has range adaptation based on population statistics, and thus the population is reinitialized every N generations so that the search region adapts toward more promising regions. Because of the reinitialization, ARMOGA can be used with a small population size similar to Micro-GA [8]. ARMOGA can be used to obtain the nondominated solutions efficiently because of the concentrated search of the probable design space, while keeping diversity.

In the present ARMOGA, the fitness value of each solution is determined by Fleming and Fonseca's Pareto-ranking method coupled with the fitness sharing approach [9]. Each individual is assigned a rank according to the number of individuals dominating it. The assigned fitness values are divided by the niche count, which is calculated by summing the sharing function values. To find the Pareto solutions more effectively, the so-called best-N selection [10] is also implemented. After determination of shared fitness values for all individuals, the stochastic universal selection (SUS) [11] is applied to select better solutions for producing a new generation. Blended crossover (BLX-α) [12] and polynomial mutation methods [13] are adopted for crossover and mutation.

E. Evaluation Method

The optimizer generates eight individuals per generation [8] and evaluates aerodynamic and structural properties of each design candidate as follows:

1) Structural optimization is performed to the jig shape to realize the minimum wing weight with constraints of strength and flutter requirements using NASTRAN. And then, the weights of the wing box and the carried fuel are calculated.

2) Static aeroelastic analysis is performed at three flight conditions to determine the aeroelastic deformed shapes (1G shape) using the Euler solver and NASTRAN.

3) Aerodynamic evaluations are performed for the 1G shapes using the Navier–Stokes solver.

4) Flight envelope analysis is performed using the properties obtained as above to evaluate the objective functions. Using the objective functions, the optimizer generates new individuals for the next generation via genetic operations, such as selection, crossover, and mutation.

The conceptual flowchart for the present MDO system is shown in Fig. 2. In the present study, MSC. NASTRAN$^{\text{TM}**}$ which is a

Table 1 Detail of design variables

Serial no.	Correspondent design variable	
1–9	PARSEC airfoil	35.0% semispan location (x_{up}, z_{up}, $z_{xx_{\text{up}}}$, x_{lo}, z_{lo}, $z_{xx_{\text{lo}}}$, α_{TE}, β_{TE}, $r_{\text{LE}_{\text{lo}}}/r_{\text{LE}_{\text{up}}}$)
10–18	PARSEC airfoil	55.5% semispan location
19–27	PARSEC airfoil	77.5% semispan location
28–33	Twist angle	19.3%, 27.2%, 35.0%, 55.5%, 77.5%, 96.0%
34, 35	Dihedral	35.0%, 96.0%

**Data available online at http://www.mscsoftware.com/ [cited 14 September 2004].

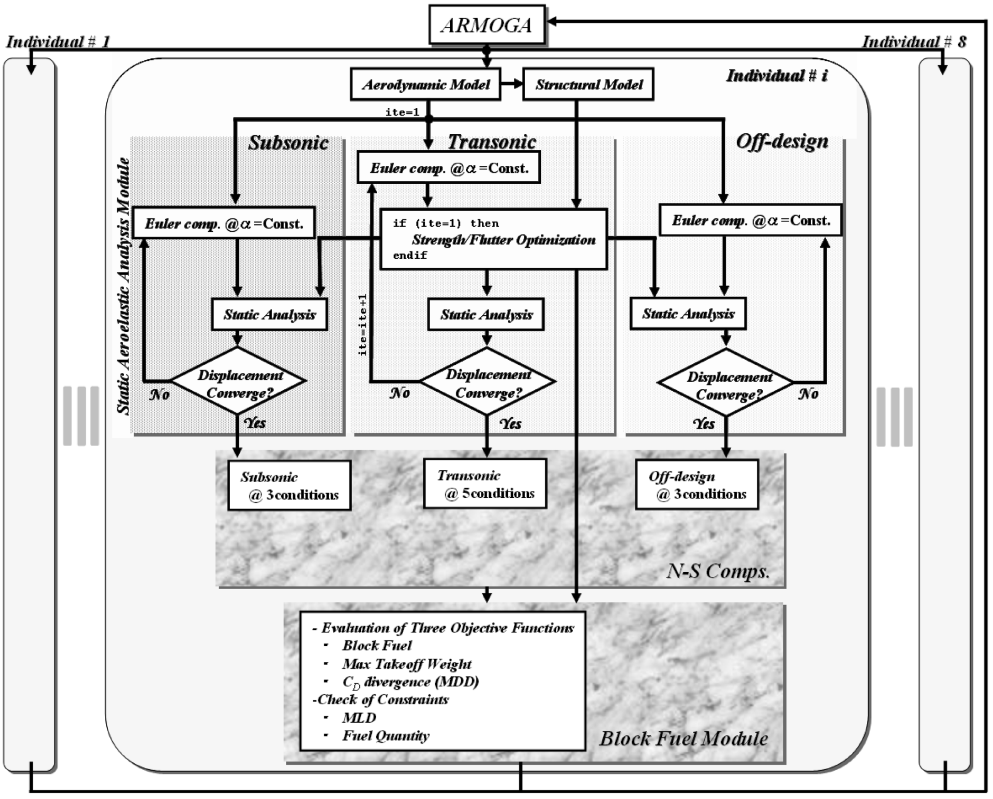

Fig. 2 Flowchart of the present MDO system.

high-fidelity commercial software is employed for the structural and aeroelastic evaluations. Besides, the inhouse unstructured mesh solver named TAS code (Tohoku University aerodynamic simulation code) [14,15] is used to evaluate aerodynamic performance using Euler and NS equations.

1. *Structural Optimization*

In the present MDO system, structural optimization of a wing box is performed to realize minimum weight with constraints of strength and flutter requirements. Given the wing outer mold line for each individual, the finite element model of the wing box is generated automatically by the finite element method (FEM) generator for the structural optimization. The wing box model mainly consists of shell elements representing skin, spar, and rib, and other wing components, such as control surfaces and subsystems, etc., are modeled using concentrated mass element. In the present structural optimization, strength and flutter characteristics are evaluated using MSC. NASTRAN.

For the strength evaluation, the static load is calculated from the pressure distribution on the wing, which is computed by the Euler solver, assuming the 4.5G upgust condition, and then static analysis is conducted where the static load acts on the wing box structure to obtain the stress on each element. For the flutter evaluation, a doublet-lattice method [16] is used to compute the unsteady aerodynamic forces on the wing, and the p–k method [17] is employed as a flutter solution to obtain the critical flutter velocity.

The present structural optimization is based on the following optimality criteria:

1) For strength optimization

$$\frac{\sigma_i}{F_i} = \text{const} \tag{1}$$

2) For flutter optimization

$$\frac{\partial V_F}{\partial t_i} = \text{const} \tag{2}$$

where σ_i denotes the stress for the ith element, F is the allowable stress, and V_F is the flutter velocity. In the structural optimization, the thickness of the shell elements is resized iteratively until the weight change is converged sufficiently under the strength and flutter constraints. The resizing formula is as follows:

1) Strength optimization

$$t_i^{\text{new}} = \frac{t_i^{\text{old}}}{(\gamma_{\min})_i} \tag{3}$$

2) Flutter optimization

$$t_i^{\text{new}} = t_i^{\text{old}} \cdot \sqrt{\frac{\partial V_F/\partial t_i}{(\partial V_F/\partial t_i)_{\text{target}}}} \tag{4}$$

where $\gamma_{\min}$ denotes the minimum strength factor. The strength and flutter constraints are as follows:

$$\sigma_{\text{compressive}} < F_{\text{compressive}} \tag{5a}$$

$$\sigma_{\text{tension}} < F_{\text{tension}} \tag{5b}$$

$$\sigma_{\text{shear}} < F_{\text{shear}} \tag{5c}$$

$$V_F > V_{F_{\text{required}}} \tag{5d}$$

$$t_i > t_{\min} \tag{5e}$$

Figure 3 shows the convergence history of structural optimization for the initial geometry.

2. *Static Aeroelastic Analysis*

First, in this module, Euler computation is carried out on an aerodynamic unstructured mesh. As surface pressure data can be obtained, surface force is computed using the FLEXCFD MHI

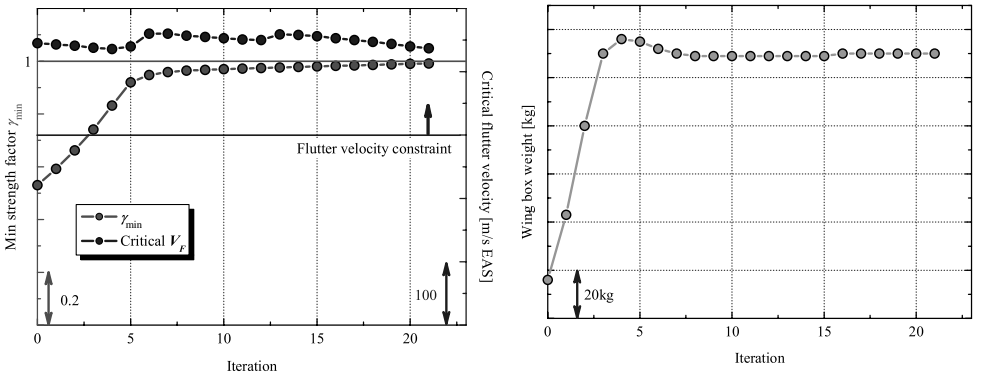

a) Strength/flutter **b) Wing box weight**

Fig. 3 Convergence histories of each characteristic for the initial geometry.

inhouse code as an interface between aerodynamics and structures. Then, the displacement is calculated from the surface force using NASTRAN. When this displacement is converged, the static aeroelastic analysis module is finished. When it is not converged, the aerodynamic mesh is moved using the unstructured dynamic mesh method [5,6] to recalculate Euler computation. As it was assumed that the planform was fixed in the present study, only displacement in the z direction was employed in the unstructured dynamic mesh method. The decision of displacement convergence was employed using the following equations:

$$\begin{cases} |C_{L(n)} - C_{L(n-1)}| \le 0.0001 & \text{if } |C_L| \text{ is small} \\ \left|\dfrac{C_{L(n)} - C_{L(n-1)}}{C_{L(n-1)}}\right| \le 0.001 & \text{otherwise} \end{cases} \tag{6}$$

The flowchart of this module is shown in Fig. 4, and the results of the static aeroelastic analysis for the initial geometry are shown in Fig. 5. The displacement computed by the present static aeroelastic analysis usually converges after three iterations.

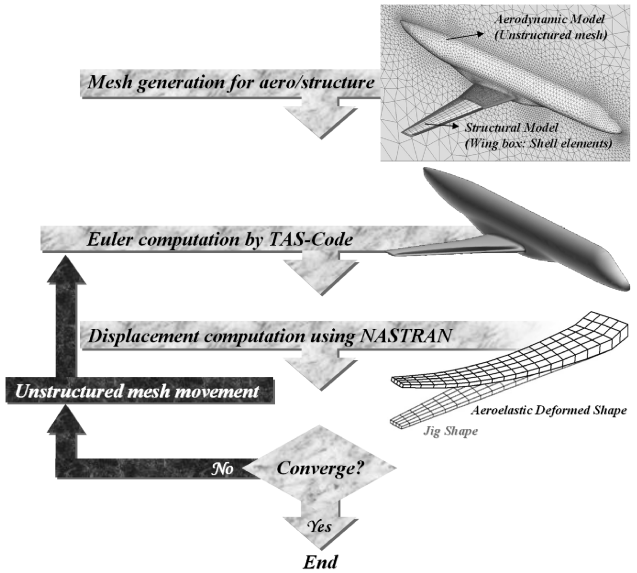

Fig. 4 Flowchart of static aeroelastic analysis. The displacement is enlarged by a factor 10 to emphasize aeroelastic deformed shape.

3. *Aerodynamic Evaluation*

In the present study, the TAS code was employed for aerodynamic evaluation. The three-dimensional Reynolds-averaged NS equations were computed with a finite-volume cell-vertex scheme. The unstructured hybrid mesh method [18] was applied to capture the boundary layer accurately and efficiently. The Harten–Lax–van Leer–Einfeldt–Wada Riemann solver [19] was used for the numerical flux computations. Venkatakrishnan's limiter [20] was applied when reconstructing the second-order accuracy. The lower–upper symmetric-Gauss–Seidel implicit scheme [21] was applied for time integration. Figure 6 shows the unstructured CFD mesh and the wing box element for the structural FEM model. For the NS computations, prism layers were stacked in 20 layers on the body surface. With regard to the turbulence model, the Spalart–Allmaras one-equation model modified by Dacles-Mariani et al. [22] was employed without transition. This model was confirmed to be effective for capturing the complex vortex structure [23]. When NS computation was carried out on the above computational condition for the initial geometry, its aerodynamic performance corresponded to the result using another solver on structured mesh.

Euler and NS computations were carried out under subsonic and transonic flight conditions, respectively. Taking advantage of the

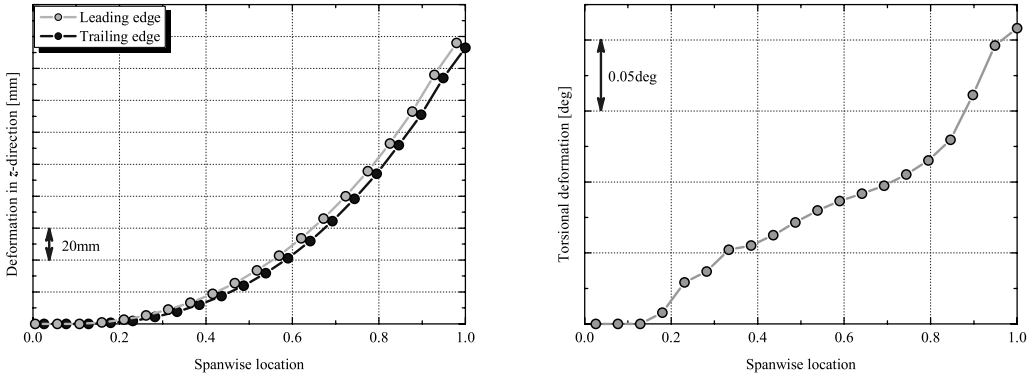

a) Deformation in z direction at leading/trailing edge **b) Torsional deformation (positive: pitch-up)**

Fig. 5 Static aeroelastic deformation of the initial geometry.

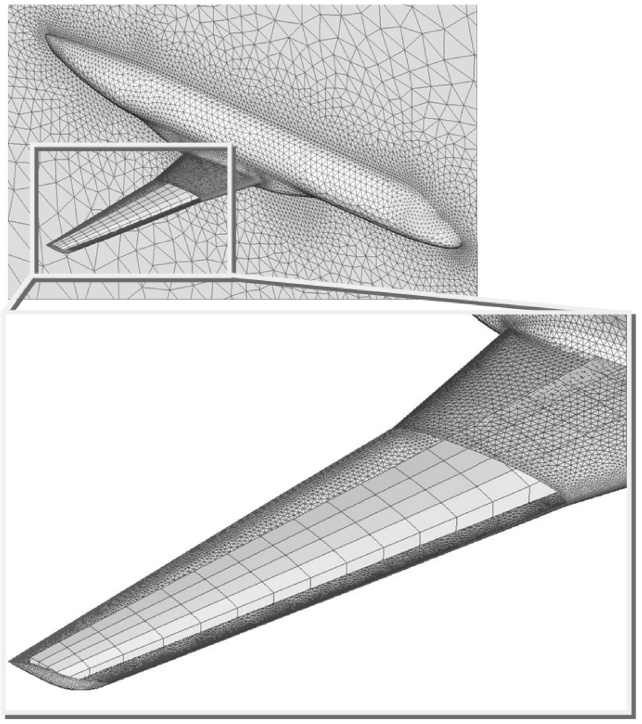

Fig. 6 Visualization between unstructured surface mesh for aerodynamic CFD model and wing box element for structural FEM model.

parallel search in EAs, the present optimization was parallelized on vector-parallel machines (NEC SX-5 and SX-7). The master processing element (PE) managed ARMOGA, while the slave PEs computed aerostructural evaluation processes. Slave processes did not require synchronization.

4. Flight Envelope Analysis

Finally, the block fuel module was executed to evaluate three objective functions as block fuel, maximum takeoff weight, and drag divergence, and to check the constraints for flight conditions shown in Fig. 2. In this module, the wing box weight for structural-optimized shape and aerodynamic performance were used as input. As all eight individuals were evaluated, the work of the slave PEs was finished in one generation.

III. Optimization Results

The population size was set to eight, and then roughly 70 Euler and 90 NS computations were performed in one generation. It took roughly 1 h of CPU time for single Euler computation, and it also took roughly 9 h for single NS computation on NEC Company SX-5 and SX-7 vector machines per PE. The population was reinitialized every five generations for the range adaptation. First, evolutionary computation was performed for 17 generations. Then, the evolutionary operation was restarted using eight nondominated solutions extracted from all solution of the 17 generations, and two more generations were computed. A total evolutionary computation of 19 generations was carried out. The evolution may not converge yet. However, the results were satisfactory because several nondominated solutions achieved significant improvements over the initial design. Furthermore, a sufficient number of solutions was searched such that the sensitivity of the design space around the initial design could be analyzed. This will provide useful information for designers.

All solutions evaluated are shown in Fig. 7, and Fig. 8 shows all solutions projected on a two-dimensional plane between two objectives, the block fuel, and the drag divergence. As this figure shows that the nondominated front was generated, there was a tradeoff between the block fuel and the drag divergence. All solutions projected on two-dimensional planes between other

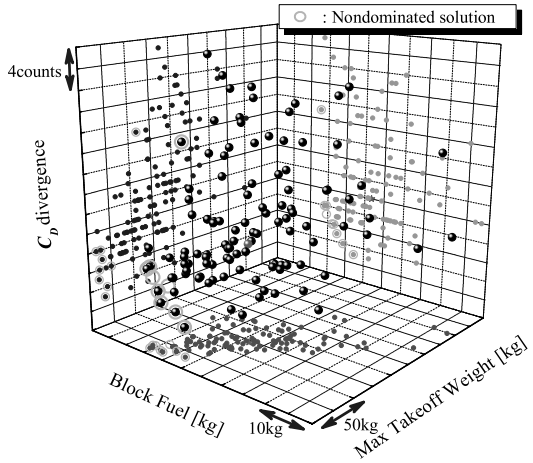

Fig. 7 All solutions plotted in three-dimensional space of all objective functions.

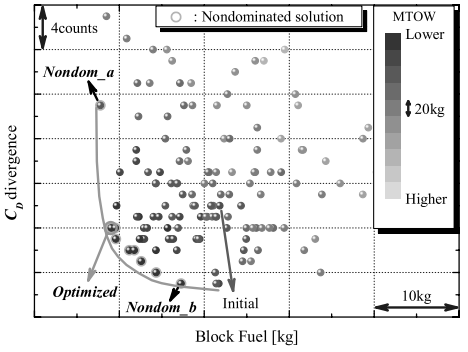

Fig. 8 All solutions on a two-dimensional plane between block fuel and C_D divergence.

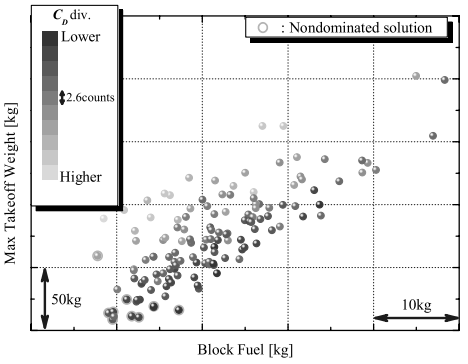

Fig. 9 All solutions on a two-dimensional plane between block fuel and maximum takeoff weight.

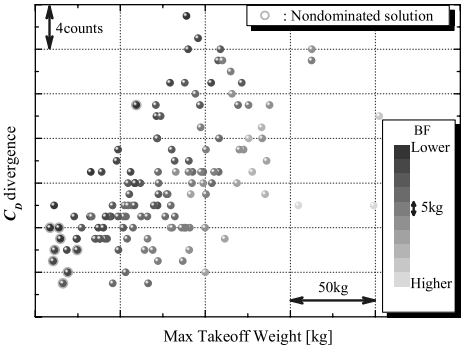

Fig. 10 All solutions on a two-dimensional plane between maximum takeoff weight and C_D divergence.

combinations were shown in Figs. 9 and 10. As the nondominated solutions did not comprise a Pareto front, these figures showed that there was no global tradeoff between these combinations of the objective functions.

A. Comparison Between Initial and Optimized Geometries

Although the wing box weight tends to increase as compared with that of the initial geometry, the block fuel can be reduced. Thus, the aerodynamic performance can redeem the penalty due to the structural weight. An individual on the nondominated front shown in Fig. 8 was selected, indicated as *optimized*, and then the optimized geometry was compared with the initial geometry.

Figure 11 shows each displacement obtained by static aeroelastic analysis. This figure shows that the displacements were not markedly different between upward and downward on the leading and trailing edges. Whereas, twisting displacement was slightly reduced in the vicinity of the kink at the 35.0% spanwise location, and then the outboard wing was bent upward as a whole. These phenomena predict reduction of the shock wave near the kink, that is, reduction of wave drag, and an increase in the generation of C_L at the outboard wing.

Figures 12 and 13 show a comparison of polar curves. Although the drag minimization was not considered here, C_D was reduced. The sensitivity of aerodynamic performance, such as C_L, C_D, and C_{Mp}, to angle of attack α did not depend on Mach numbers very much. By comparison of the polar curves at constant C_L for the cruising condition, C_D of the optimized geometry was found to be reduced by 5.5 counts. Because of the improvement of the drag, the block fuel of the optimized geometry was decreased by over 1% even with its structural weight penalty.

Next, the mechanism of the drag reduction was investigated. Figure 14 shows a comparison of the spanwise distributions of C_L and C_D of the initial and optimized geometries. This figure shows that the drag decreased at the 35.0% spanwise location. Figure 15 shows a comparison of the pressure distributions at the 35.0% spanwise location. Then, the variation in the leading-edge bluntness works to depress the shock wave on the upper wing surface, that is, to reduce the wave drag. In fact, the pressure drag coefficient was reduced by 5.6 counts. Figure 16 shows a comparison of the shock wave visualized by the shock function F_{shock} [24], which is given as follows:

$$F_{\text{shock}} = \frac{\boldsymbol{V} \cdot \nabla P}{a \cdot |\nabla P|} \tag{7}$$

where $\boldsymbol{V}$ is the velocity vector, P is pressure, and a denotes the local speed of sound.

The shock wave of the optimized geometry was weaker than that of the initial geometry in the vicinity of the 35.0% spanwise location as shown in Fig. 16 indicating the wave drag reduction. Moreover, the vorticity of the wing wake of the optimized geometry in the vicinity of the 35.0% spanwise location was weaker than that of the initial geometry as shown by helicity contours in Fig. 17. Therefore, these figures show that the shape change near the 35.0% spanwise location, that is, the shape modification in the vicinity of the kink is effective to reduce the drag. Figure 17 also shows strong vortices in

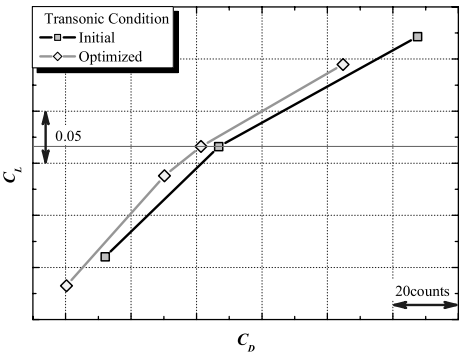

Fig. 13 Comparison of the C_L–C_D curves between initial and optimized geometries under the transonic flight condition.

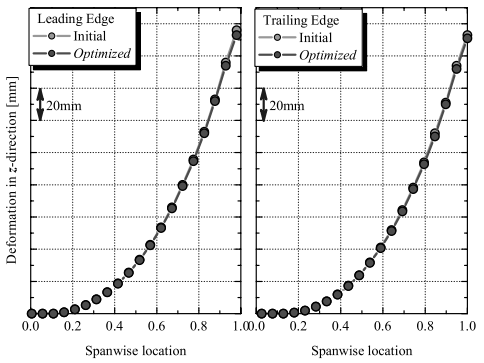

a) Deformation in z direction at leading/trailing edge

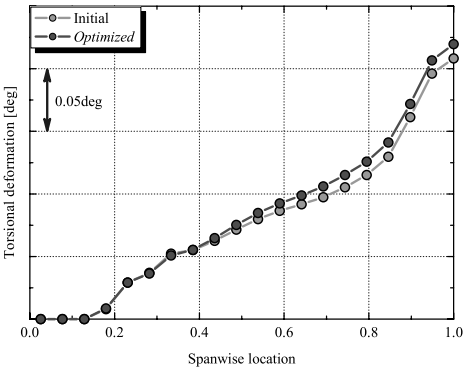

b) Torsional deformation (positive: pitch-up)

Fig. 11 Comparison of static aeroelastic deformation between initial and optimized geometries.

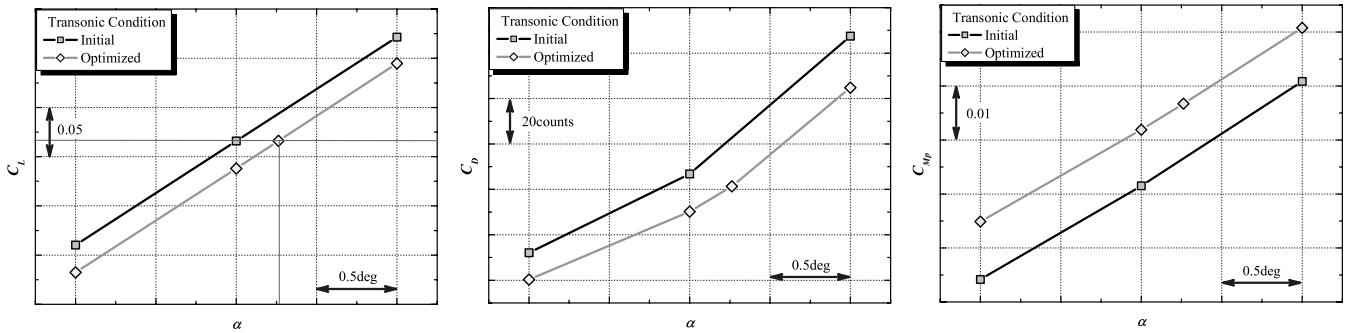

Fig. 12 Comparison of the C_L–α, C_D–α, and C_{Mp}–α curves between initial and optimized geometries under the transonic flight condition.

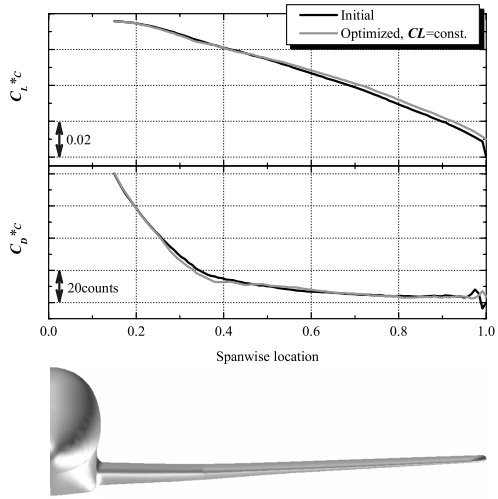

Fig. 14 Comparison of C_L and C_D spanwise distributions between initial and optimized geometries under the transonic cruising flight condition. C_L is constant.

the vicinity of the fairing. Thus, improvement of the fairing design should be considered in the future.

B. Comparison Between Weak Nondominated Solutions with Regard to Block Fuel

Figures 8–10 show that there is a tradeoff only between block fuel and C_D divergence. To investigate the geometric sensitivity to the primary objective, block fuel, aerodynamic performance was compared between weak nondominated solutions. Left-side and right-side weak nondominated solutions are named as "Nondom_a" and "Nondom_b," respectively, in Fig. 8.

Figure 18 shows displacements obtained by static aeroelastic analysis. This figure shows no marked differences in upward or downward displacements on both the leading and trailing edges. However, there was a difference in twisting between the 50–85% spanwise location. Figures 19 and 20 show the polar curves under subsonic and transonic flight conditions. C_L–C_D curves of both flight conditions appear very similar. It should be noted that C_D is more sensitive to α. Although there were no differences in the sensitivity of C_L and C_{Mp} to α, the increase ratios of C_D were different as shown in C_D–α curves in Fig. 14. This tendency was pronounced more when the Mach number increased. This result indicated that the C_D increase follows the C_L increase to achieve an increase in L/D. In fact, Nondom_a geometry showed an L/D increase of roughly 3.2% at the cruise condition as compared with Nondom_b. Therefore, under subsonic and transonic flight conditions, L/D is found highly related to block fuel improvements. Especially, transonic L/D was more sensitive because of its nonlinearity in α.

The mechanism of L/D increase depends on the bluntness of the upper surface of the leading edge. The PARSEC design variable $r_{\mathrm{LE_{lo}}}/r_{\mathrm{LE_{up}}}$, which is the leading-edge bluntness ratio between the lower and upper surfaces, for Nondom_a was one-tenth higher than the value for Nondom_b at the 35.0% spanwise location. Therefore, the curvature of Nondom_b was smaller, the shock wave becomes weaker, and then the wave drag was reduced. Figure 21 shows C_p distributions at three spanwise locations. The shock wave on the wing of Nondom_b as a whole was clearly depressed. This result was also confirmed on the shock wave visualization shown in Fig. 22.

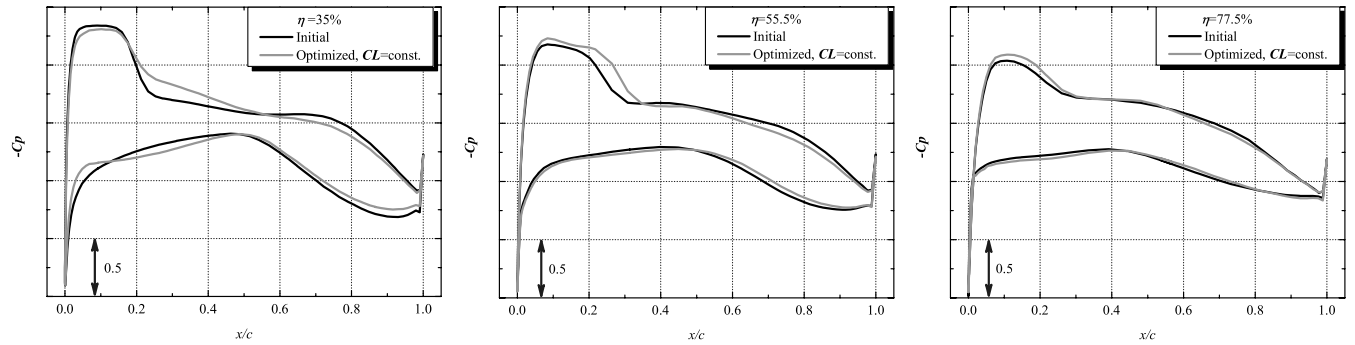

Fig. 15 Comparison of C_p distributions between initial and optimized geometries under the transonic cruising flight condition at 35.0, 55.5, and 77.5% semispan locations, respectively. C_L is constant.

Fig. 16 Comparison of shock wave visualizations colored by entropy under the transonic cruising flight condition between initial (left) and optimized (right) geometries. C_L is constant.

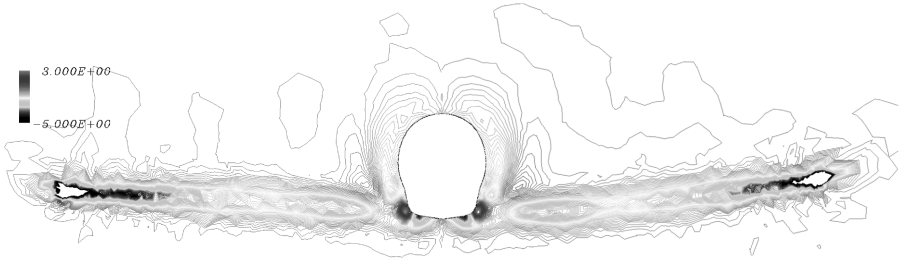

Fig. 17 Comparison of helicity contours of wing wake of $x/L = 0.7$ under the transonic cruising flight condition between initial (left) and optimized (right) geometries. C_L is constant. The vortical rotation direction is colored symmetrically.

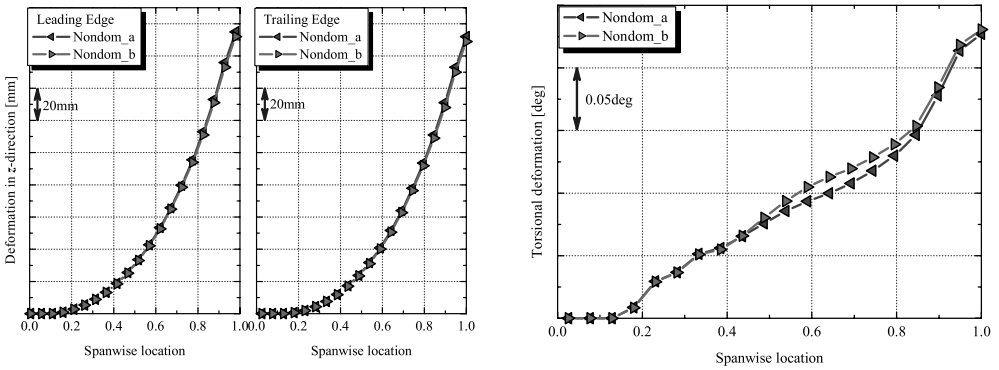

a) Deformation in z direction at leading/trailing edge **b) Torsional deformation (positive: pitch-up)**

Fig. 18 Comparison of static aeroelastic deformation between weak nondominated solutions.

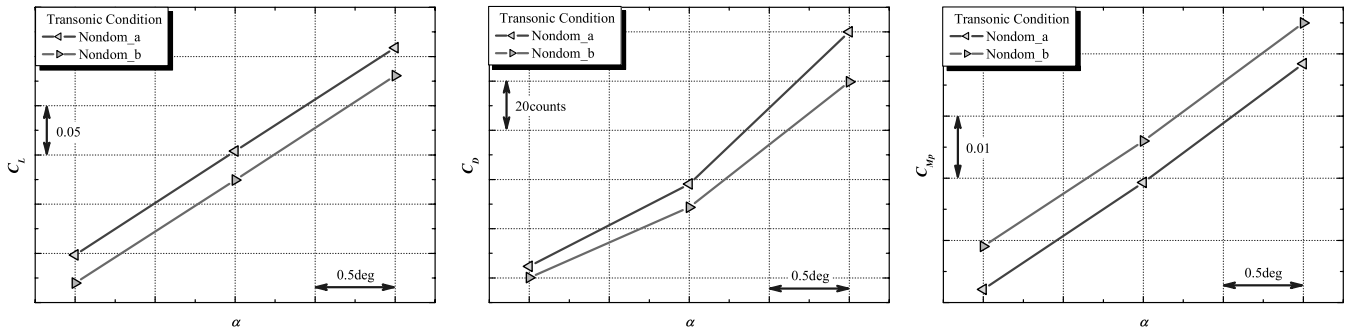

Fig. 19 Comparison of the C_L–α, C_D–α, and C_{Mp}–α curves between weak nondominated solutions geometries under the transonic cruising flight condition.

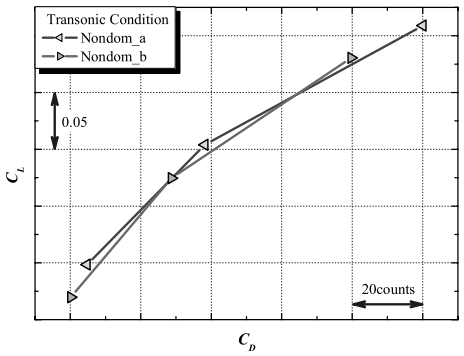

Fig. 20 Comparison of the C_L–C_D curves between weak nondominated solutions under the transonic cruising flight condition.

However, helicity contours did not show a clear distinction in Fig. 23. Thus, the C_D decrease may be dependent only on the wave drag.

IV. Data Mining

If the optimization problem has only two objectives, tradeoffs can be visualized easily. However, if there are more than two objectives, the technique to visualize the computed nondominated solutions is needed. Therefore, in the present study, self-organizing maps (SOMs) proposed by Kohonen [25] were employed. SOM is a technique not only for visualization but also a tool for the intelligent compression of information. That is, SOM can be applied for data mining to acquire knowledge regarding the design space. In the present study, Viscovery® SOMine[††] (Eudaptics GmbH, Austria) was employed.

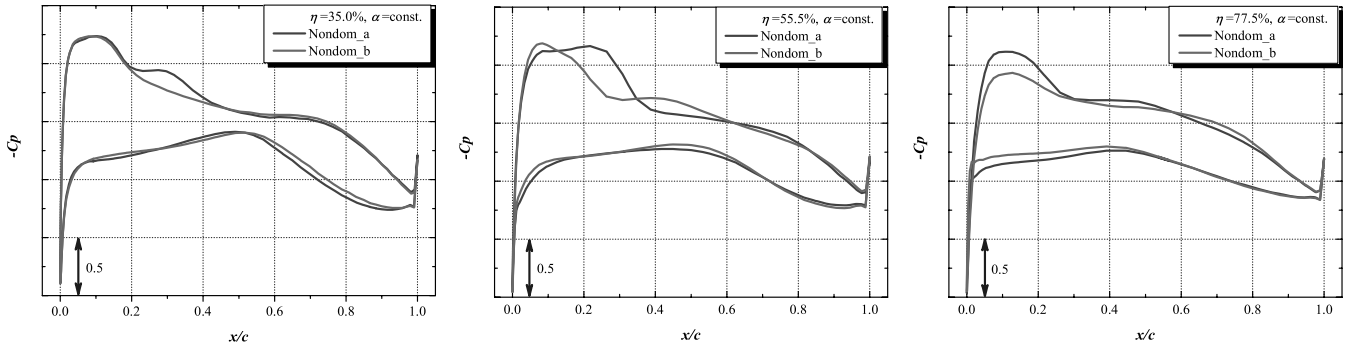

Fig. 21 Comparison of the pressure distributions between weak nondominated solution geometries under the transonic cruising flight condition at 35.0, 55.5, and 77.5% semispan locations, respectively.

[††]"Eudaptics" available online at http://www.eudaptics.com [cited 16 June 2004].

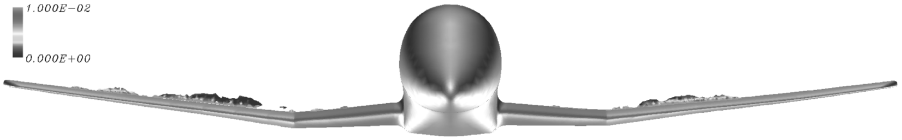

Fig. 22 Comparison of shock wave visualizations colored by entropy under the transonic cruising flight condition between weak nondominated solutions of nondom_a (left) and nondom_b (right) geometries.

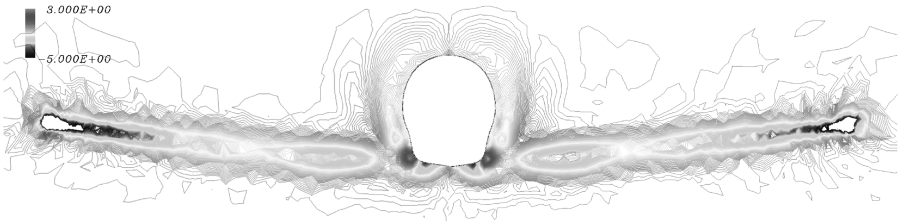

Fig. 23 Comparison of helicity contours of wing wake of $x/L = 0.7$ under the transonic cruising flight condition between weak nondominated solutions of nondom_a (left) and nondom_b (right) geometries. The vortical rotation direction is colored symmetrically.

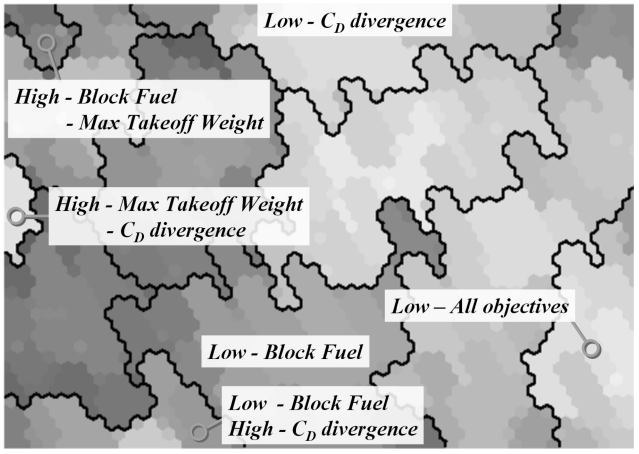

Fig. 24 SOM of all solutions in the three-dimensional objective function space.

A. Knowledge in the Design Space

1. *Tradeoff Analysis of the Design Space*

All of the solutions have been projected onto the two-dimensional map of SOM. Figure 24 shows the resulting SOM with 11 clusters considering the three objectives. Furthermore, Fig. 25 shows the SOMs colored by the three objectives. These color figures show that the SOM indicated in Fig. 24 can be grouped as follows: The upper left corner corresponds to the designs with high block fuel and maximum takeoff weight. The left center area corresponds to designs with high maximum takeoff weight and C_D divergence. The lower left corner corresponds to designs with low block fuel and high C_D divergence. Figures 25a and 25c show that there is a tradeoff between these two objective functions. The lower center area corresponds to designs with low block fuel. The right-hand side corresponds to designs with low C_D divergence. As the coloring in Fig. 25a is similar to that in Fig. 25b, there was not a severe tradeoff between the block fuel and the maximum takeoff weight. The lower right corner corresponds to designs with low value of all objectives. Extreme nondominated solutions are indicated in Figs. 25a–25c. As they are in different clusters, the simultaneous optimization of the three objectives is impossible. However, the lower right cluster has relatively low values for all three objectives. Thus, this region of the design space may provide a sweet spot for the present design problem.

2. *Additional Characteristics*

Figure 26 shows the SOM colored by three other characteristic values. Figure 26a shows the SOM colored by the constraints of the evaluated fuel mass. The colored values are defined as follows:

$$\text{value} = \text{volume}_{\text{required fuel}} - \text{volume}_{\text{fuel capacity}} \tag{8}$$

where $\text{volume}_{\text{required fuel}}$ denotes the fuel volume required to fly the given range, and $\text{volume}_{\text{fuel capacity}}$ denotes the fuel capacity volume that can actually be carried in the wing. When this value is greater than zero, the aircraft cannot fly the given range. As the area with values of over zero corresponds to the area with high maximum takeoff weight, the aerodynamic characteristics and design values that have effects on maximum takeoff weight dominate this constraint.

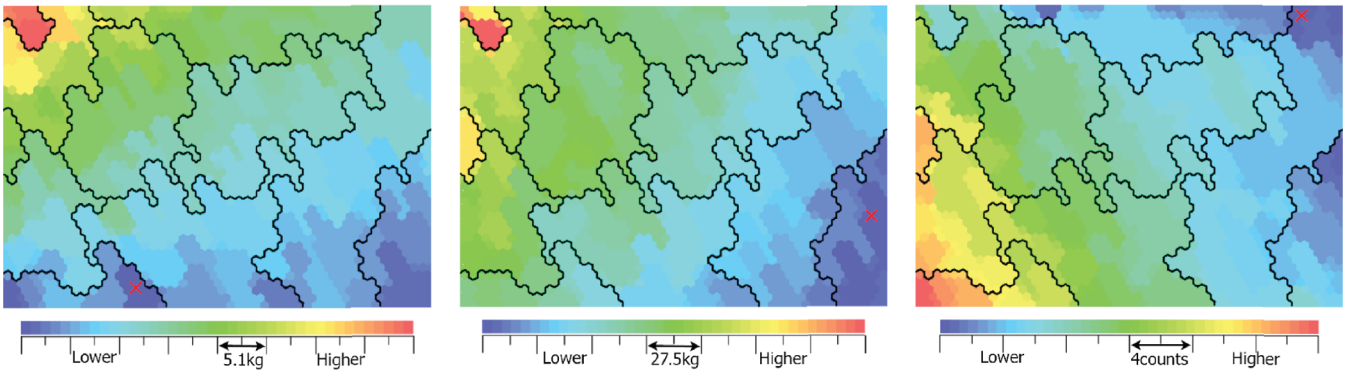

a) SOM colored by the block fuel as the objective function 1

b) SOM colored by the max takeoff weight as the objective function 2

c) SOM colored by the C_D divergence as the objective function 3

Fig. 25 SOM colored by the objective functions. The symbol × denotes the respective extreme nondominated solutions.

Figure 26b shows the SOM colored by the ranking in the optimizer. As the upper left region has a poorer ranking, larger block fuel and maximum takeoff weight as objective functions 1 and 2 dominate the poor ranking. In contrast, the lower left area with higher C_D divergence does not have poor ranking. These observations indicate that improvement in C_D divergence is not dominated by the specific aerodynamic performance and design variables, and further improvement cannot be achieved by the present problem easily.

Figure 26c shows the SOM colored by the angle between inboard and outboard on the upper wing surface for the gull wing at the kink location. Angles greater and less than 180 deg correspond to gull and inverted gull wing, respectively. The locations of higher values of this angle as shown in Fig. 26c correspond to positions of higher C_D under the transonic cruising flight condition shown in Fig. 27b. However, at angles less than 180 deg, there was little correlation between Figs. 26c and 27b. The inverted gull wing did not affect aerodynamic performance. The inverted gull wing is known to have a structural weight increase, which is also observed in the present results. Indeed, the locations of higher angles in Fig. 26c had higher maximum takeoff weights as shown in Fig. 25b. Therefore, nongull wings should be designed in the future.

3. *Effects of Design Variables*

Finally, Figs. 28 and 29 show the SOMs colored by the selected design variables with regard to the PARSEC airfoil parameters at

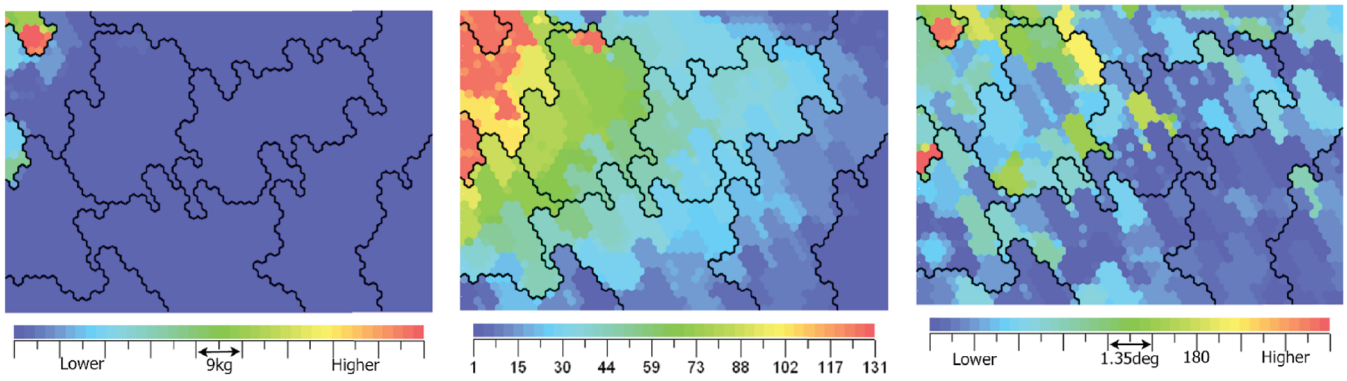

a) SOM colored by the constraint as wing box volume **b) SOM colored by the ranking in the optimizer** **c) SOM colored by the angle on upper surface expressing the gull wing at kink location**

Fig. 26 SOM colored by the characteristic values.

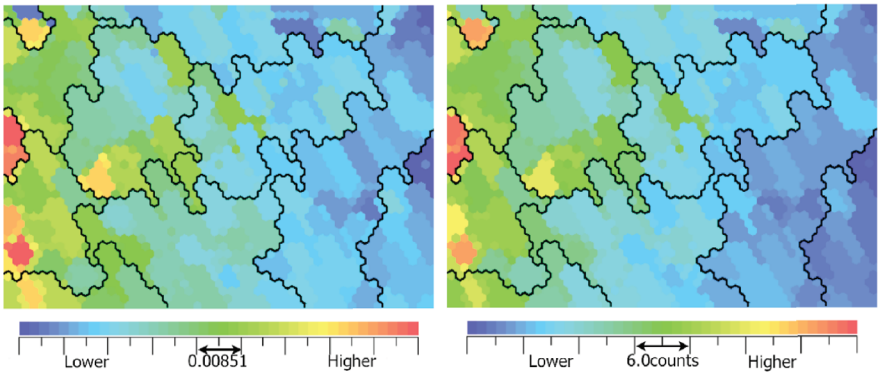

a) SOM colored by C_L **b) SOM colored by C_D**

Fig. 27 SOM colored by aerodynamic performance under the transonic cruising flight condition.

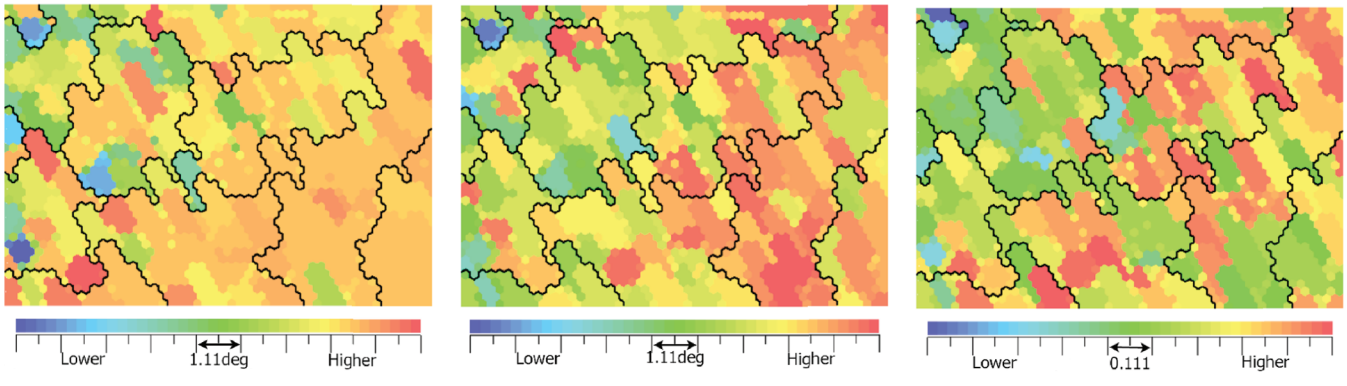

a) SOM colored by PARSEC α_{TE} **b) SOM colored by PARSEC β_{TE}** **c) SOM colored by PARSEC $r_{LE_{lo}}/r_{LE_{up}}$**

Fig. 28 SOM colored by characteristic design variables regarding the PARSEC airfoil at 35.0% spanwise location. The minimum and maximum values of the color bar are set using the minimum and maximum values of each design variable in the optimizer, respectively.

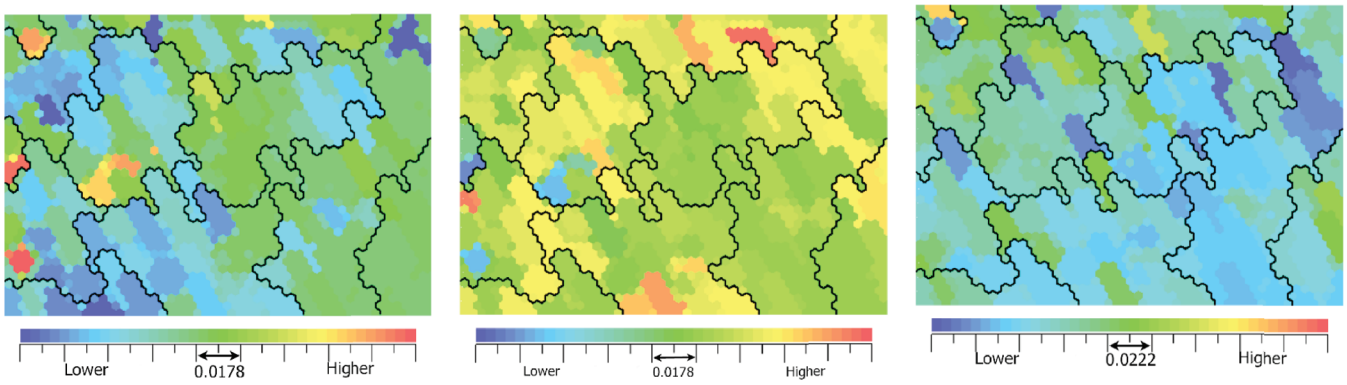

a) SOM colored by PARSEC x_{up} **b) SOM colored by PARSEC x_{lo}** **c) SOM colored by PARSEC $z_{xx_{lo}}$**

Fig. 29 SOM colored by the characteristic design variables regarding the PARSEC airfoil at 55.5% spanwise location. The minimum and maximum values of the color bar are set using the minimum and maximum values of each design variable in the optimizer, respectively.

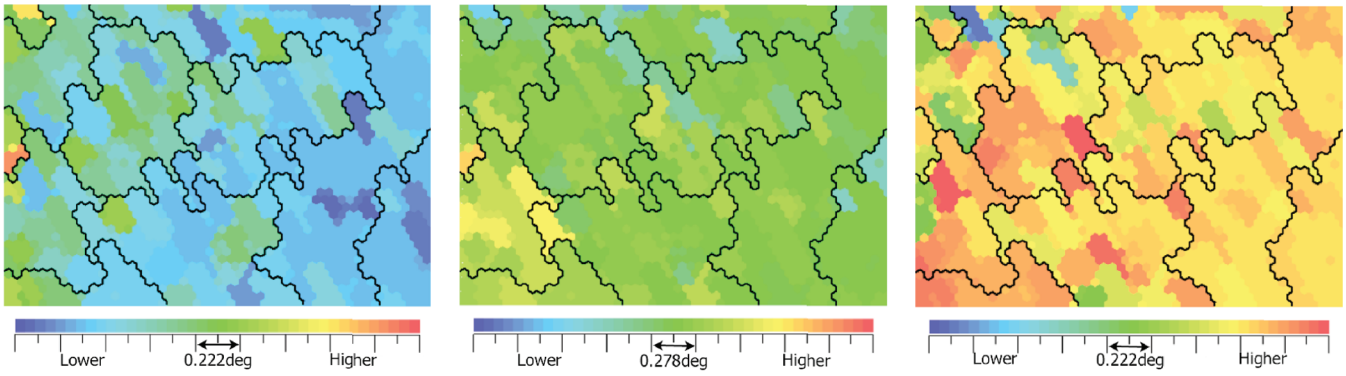

a) SOM colored by the twist angle at 35.0% spanwise location **b) SOM colored by the twist angle at 55.5% spanwise location** **c) SOM colored by the twist angle at 96.0% spanwise location**

Fig. 30 SOM colored by the characteristic design variables involving wing twist. The minimum and maximum values of the color bar are set using the minimum and maximum values of each design variable in the optimizer, respectively.

35.0 and 55.5% spanwise locations, respectively. Moreover, Fig. 30 shows the SOM colored by the design variable, twist angle. The design variables can be summarized as follows, taking into consideration the effects on each objective function and aerodynamic performance.

There are no design variables that show large effects on objective function 1 as block fuel. The large twist angles at the 35.0% spanwise location make objective function 2 as maximum takeoff weight worse. In addition, large twist angles at the 55.5% spanwise location increase objective function 3 as C_D divergence. However, no design variable of the PARSEC airfoil had apparent effects on any objective functions by itself. As shown later, PARSEC design variables have direct effects on aerodynamic performances. However, the present objective functions are not pure aerodynamic characteristics. Therefore, effects of the design variables on the objective functions were not trivial. There were no design variables and no aerodynamic characteristics that were effective on the sweet spot with relatively low values for all three objective functions. Therefore, the individual that resides in the sweet spot cannot be generated by hand. A correlation between objective function and design variable is desirable when the sensitivity of the design variable is to be investigated; this is one of the important aspects in optimization problems in general.

Next, the effects of design variables on aerodynamic performance were investigated. From the correspondence between Figs. 27–30, the effects of respective design variables are summarized in Tables 2–4. These tables indicate that the design variables of the PARSEC airfoil have effects on aerodynamic performance directly. It is noted that the effects of design variables to C_D can be predicted from the above results because Figs. 27a and 27b are similar. Furthermore, the effects of design variables on aerodynamic

Table 2 Effects of design variables to C_L under the transonic cruising flight condition

Design variable		C_L
PARSEC α_{TE} @ 35.0%	Decrease	Increase
PARSEC x_{up} @ 55.5%	Increase	Increase
PARSEC x_{lo} @ 55.5%	Decrease	Increase
Twist @ 35.0%	Increase	Increase
Twist @ 55.5%	Increase	Increase

Table 3 Effects of design variables to L/D under the transonic cruising flight condition

Design variable		L/D
PARSEC $r_{LE_{lo}}/r_{LE_{up}}$ @ 35.0%	Decrease	Decrease
PARSEC $z_{xx_{lo}}$ @ 55.5%	Increase	Decrease

Table 4 Effects of design variables to C_{Mp} under the transonic cruising flight condition

Design variable		C_{Mp}
PARSEC α_{TE} @ 35.0%	Decrease	Decrease
PARSEC β_{TE} @ 35.0%	Decrease	Decrease
PARSEC $r_{LE_{lo}}/r_{LE_{up}}$ @ 35.0%	Decrease	Increase
PARSEC x_{up} @ 55.5%	Increase	Decrease
PARSEC x_{lo} @ 55.5%	Decrease	Decrease
PARSEC $z_{xx_{lo}}$ @ 55.5%	Increase	Increase

performance under the subsonic flight condition can be predicted because the SOMs appeared similar at the transonic and subsonic flight conditions. The leading-edge curvature of PARSEC airfoil at the 35.0% spanwise location was effective to L/D and C_{MP}.

The geometry near the 55.5% spanwise location was not changed markedly with regard to the twist angle, as shown in Fig. 30b. The geometry near the 96.0% spanwise location was changed to upward twisting. Conversely, the geometry near the 35.0% spanwise location was changed to downward twisting. The improvement in the vicinity of the 35.0% spanwise location restrained the shock wave, reducing the wave drag shown in Fig. 16. When the drag decreases, the lift may decrease simultaneously. The lift was increased to compensate for the reduction in the vicinity of the kink so that the angle of attack of the outboard wing was increased although the wing is still twisted down. It should be noted that the angle of attack near the kink had an effect on the transonic drag, especially as shown in Fig. 30a. This corresponds to the phenomena shown in Fig. 16. Specifically, the shock wave in the vicinity of the kink is weakened. The angle of attack near the kink with downward twisting is replaced from the initial geometry and the lost lift is made up to replace the angle of attack at the outboard wing with upward twisting so that the wave drag is reduced near the kink. Upward twisting at the outboard wing has no influence on transonic drag, as shown in Fig. 30c. This corresponds to the prediction shown in Fig. 11. The other design variables were not effective to reduce the objective functions or to increase aerodynamic performance as C_D and L/D under transonic cruise flight condition. Data mining techniques using SOM were found to be able to classify the design variables considering their influence on the objectives and aerodynamic performance.

Design knowledge regarding the block fuel, which is the most important element of the present optimization problem, will be considered. The following two points are the keys to improve the block fuel: 1) L/D increase, and 2) $dC_D/d\alpha$ increase, at any Mach number. However, there were no single design variable in the present design space capable of satisfying them simultaneously. In fact, this was confirmed by the SOMs. Although PARSEC design variables correspond to aerodynamic performances, there are no direct effects on other objective functions. It would be easier to understand the design space if the design variables have direct influences on the objective functions.

B. Evaluation of the Nongull Geometry

The design knowledge obtained by SOM shows that a nongull wing should be designed. Therefore, we modified the optimized wing shape which achieved the higher improvement in the block fuel to the nongull-wing shape (called "optimized_mod") to verify the design knowledge obtained by the previous data mining.

The result is shown in Figs. 31–33. These figures show that optimized_mod improves both block fuel and maximum takeoff weight. Moreover, by comparison of the polar curves at constant C_L for the cruising condition shown in Fig. 34, C_D of optimized_mod was found to be reduced by 10.6 counts over the initial geometry. Because of the improvement of drag, the block fuel of optimized_mod was reduced by 3.6%.

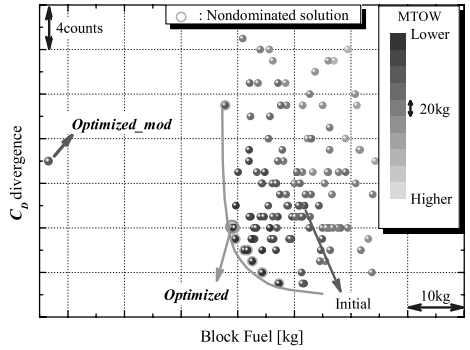

Fig. 31 Comparison of optimized_mod and all solutions on the two-dimensional plane between block fuel and C_D divergence.

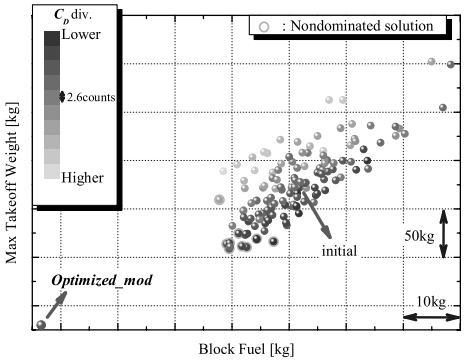

Fig. 32 Comparison of optimized_mod and all solutions on the two-dimensional plane between block fuel and maximum takeoff weight.

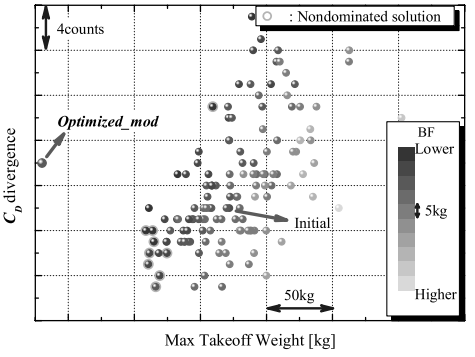

Fig. 33 Comparison of optimized_mod and all solutions on the two-dimensional plane between maximum takeoff weight and C_D divergence.

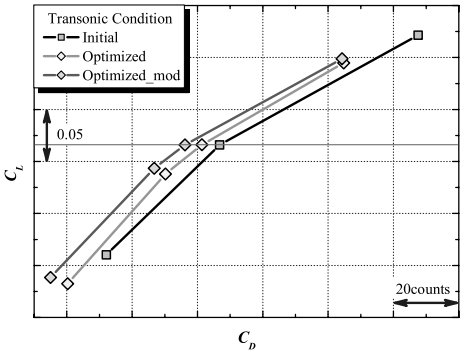

Fig. 34 Comparison of the C_L–C_D curves among three geometries as initial, optimized, and optimized_mod under the transonic flight condition.

In the present MDO system, surface spline function of the geometry deviation ΔZ was used for the modification of the wing shape (surface mesh), and then the volume mesh was modified by the unstructured dynamic mesh method. However, this process made the surface mesh distorted around the leading edge and highly limited the design space shown in Fig. 35. This mesh generation process might be the primary reason for the difficulty in finding the nongull geometry with better block fuel performance. The secondary reason is that only a small number of the generations has been performed. However, this result reveals that the data mining technique salvages the information. It is demonstrated that the knowledge discovery by data mining regarding design space is an important aspect in the practical optimization.

V. Conclusions

The wing shape of a regional-jet aircraft was optimized using ARMOGA considering three aerostructural objective functions with

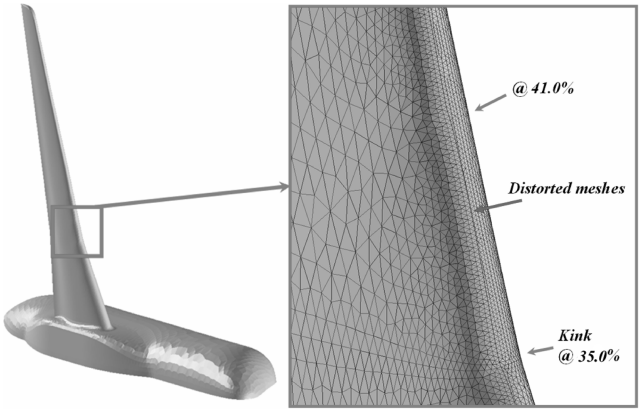

Fig. 35 Example of distorted mesh in the vicinity of the leading edge.

high-fidelity evaluations. Consequently, the objective function value considering block fuel was reduced by over 1% as compared with the initial geometry. The geometry change in the vicinity of the kink was found to be effective for drag reduction. The tradeoff information among the three objective functions was revealed, and a main tradeoff was found between the block fuel and the drag divergence.

Moreover, data mining for the design space was performed using a SOM. As a result, particular design variables effective to improve the objective functions and aerodynamic performance were found. Detailed observations of SOM revealed that there is a sweet spot in the design space where the three objectives become relatively low.

One of the key features found by data mining was the nongull-wing geometry, although the present MDO results showed the inverted gull wings as nondominated solutions. When this knowledge was applied to one optimum solution, the resulting design was found to have better performance and to achieve 3.6% improvement in the block fuel compared with the original geometry designed in the conventional manner. The data mining technique provides knowledge regarding the design space and may salvage lost information during the optimization operation, which will be an important facet of solving practical optimization problems.

Acknowledgements

We would like to thank Takano, Y. and Kumano, T., graduate students at Tohoku University for generating the CATIA™ stereo lithography and the mesh data of the initial geometry, and the optimized_mod geometry, respectively. The Euler/NS computations were performed using the NEC Company SX-5 at the Institute of Fluid Science, Tohoku University, and the NEC Company SX-7 in Super-Computing System Information Synergy Center, Tohoku University.

References

[1] Kroo, I., Altus, S., Braun, R., Gage, P., and Sobieski, I., "Multidisciplinary Optimization Methods for Aircraft Preliminary Design," AIAA Paper 94-4325-CP, 1994.

[2] Sobieszczanski-Sobieski, J., and Haftka, R. T., "Multidisciplinary Aerospace Design Optimization: Survey of Recent Developments," *Structural Optimization*, Vol. 14, No. 1, 1997, pp. 1–23.

[3] Martins, J. R. R. A., Alonso, J. J., and Reuther, J. J., "High-Fidelity Aerostructural Design Optimization of a Supersonic Business Jet," *Journal of Aircraft*, Vol. 41, No. 3, 2004, pp. 523–530.

[4] Oyama, A., Obayashi, S., Nakahashi, K., and Hirose, N., "Aerodynamic Wing Optimization via Evolutionary Algorithms Based on Structured Coding," *Computational Fluid Dynamics Journal*, Vol. 8, No. 4, 2000, pp. 570–577.

[5] Murayama, M., Nakahashi, K., and Matsushima, K., "Unstructured Dynamic Mesh for Large Movement and Deformation," AIAA Paper 2002-0122, 2002.

[6] Yamazaki, W., Matsushima, K., and Nakahashi, K., "Aerodynamic Optimization of NEXST-1 SST Model at Near-Sonic Regime," AIAA Paper 2004-0034, 2004.

[7] Sasaki, D., and Obayashi, S., "Efficient Search for Trade-Offs by Adaptive Range Multi-Objective Genetic Algorithms," *Journal of Aerospace Computing, Information, and Communication*, Vol. 2, No. 1, 2005, pp. 44–64.

[8] Krishnakumar, K., "Micro-Genetic Algorithms for Stationary and Non-Stationary Function Optimization," *SPIE Proceedings of Intelligent Control and Adaptive Systems*, Vol. 1196, SPIE, Bellingham, WA, 1989, pp. 289–296.

[9] Fonseca, C. M., and Fleming, P. J., "Genetic Algorithms for Multiobjective Optimization: Formulation, Discussion and Generalization," *Proceedings of the Fifth International Conference on Genetic Algorithms*, Morgan Kauffman, San Mateo, CA, 1993, pp. 416–423.

[10] Obayashi, S., Takahashi, S., and Takeguchi, Y., "Niching and Elitist Models for MOGAs," *Parallel Problem Solving from Nature, PPSN V*, LNCS 1498, Springer, Berlin, 1998, pp. 260–269.

[11] Baker, J. E., "Reducing Bias and Inefficiency in the Selection Algorithm," *Proceedings of the Second International Conference on Genetic Algorithms*, Lawrence Erlbam Assoc., Hillsdale, NJ, 1987, pp. 14–21.

[12] Eshelman, L. J., and Schaffer, J. D., "Real-Coded Genetic Algorithms and Interval Schemata," *Foundations of Genetic Algorithms 2*, Morgan Kaufmann, San Mateo, CA, 1993, pp. 187–202.

[13] Deb, K., *Multi-Objective Optimization Using Evolutionary Algorithms*, John Wiley & Sons, Ltd., Chichester, 2001.

[14] Ito, Y., and Nakahashi, K., "Direct Surface Triangulation Using Stereolithography Data," *AIAA Journal*, Vol. 40, No. 3, 2002, pp. 490–496.

[15] Sharov, D., and Nakahashi, K., "A Boundary Recovery Algorithm for Delaunay Tetrahedral Meshing," *Proceedings of the 5th International Conference on Numerical Grid Generation in Computational Field Simulations*, Mississippi State University, Starkville, MS, 1996, pp. 229–238.

[16] Albano, E., and Rodden, W. P., "A Doublet-Lattice Method for Calculating Lift Distributions on Oscillating Surfaces in Subsonic Flows," *AIAA Journal*, Vol. 7, No. 2, 1969, pp. 279–285.

[17] Crittenden, J. B., Weisshaar, T. A., Johnson, E. H., and Rutkowski, M. J., "Aeroelastic Stability Characteristics of an Oblique-Wing Aircraft," *Journal of Aircraft*, Vol. 15, No. 7, 1978, pp. 429–434.

[18] Ito, Y., and Nakahashi, K., "Improvements in the Reliability and Quality of Unstructured Hybrid Mesh Generation," *International Journal for Numerical Methods in Fluids*, Vol. 45, No. 1, 2004, pp. 79–108.

[19] Obayashi, S., and Guruswamy, G. P., "Convergence Acceleration of an Aeroelastic Navier-Stokes Solver," *AIAA Journal*, Vol. 33, No. 6, 1994, pp. 1134–1141.

[20] Venkatakrishnan, V., "On the Accuracy of Limiters and Convergence to Steady State Solutions," AIAA Paper 93-0880, 1993.

[21] Sharov, D., and Nakahashi, K., "Reordering of Hybrid Unstructured Grids for Lower-Upper Symmetric Gauss-Seidel Computations," *AIAA Journal*, Vol. 36, No. 3, 1998, pp. 484–486.

[22] Dacles-Mariani, J., Zilliac, G. G., Chow, J. S., and Bradshaw, P., "Numerical/Experimental Study of a Wingtip Vortex in the Near Field," *AIAA Journal*, Vol. 33, No. 9, 1995, pp. 1561–1568.

[23] Chiba, K., Obayashi, S., and Nakahashi, K., "CFD Visualization of Second Primary Vortex Structure on a 65-Degree Delta Wing," AIAA Paper 2004-1231, 2004.

[24] Yamazaki, W., "Aerodynamic Optimization of Near-Sonic Plane Based on NEXST-1 SST Model," ICAS Paper 2004-4.3.4, 2004.

[25] Kohonen, T., *Self-Organizing Maps*, Springer, Berlin, 1995.